

2001

Simulating ultrasonic sensing with the lattice gas model

P. McKerrow

University of Wollongong, phillip@uow.edu.au

S. M. Zhu

University of Wollongong

S. New

University of Wollongong

Publication Details

This article was originally published as: McKerrow, P, Zhu, S & New, S, Simulating ultrasonic sensing with the lattice gas model, IEEE Transactions on Robotics and Automation, April 2001, 17(2), 202-208. Copyright IEEE 2001.

Simulating ultrasonic sensing with the lattice gas model

Abstract

People have difficulty understanding ultrasonic sensing because they cannot see sound. The purpose of simulation is to overcome this problem by visualizing the scattering of ultrasonic waves off objects. The lattice gas model calculates wave behavior with finite difference equations to produce data suitable for grayscale visualization. This visualization is useful when designing ultrasonic sensing systems for navigating mobile robots. Situations that result in the sensor failing to detect an object can be studied with the simulator.

Keywords

control engineering computing, data visualisation, digital simulation, finite difference methods, lattice gas, mobile robots, navigation, ultrasonic measurement, ultrasonic scattering

Disciplines

Physical Sciences and Mathematics

Publication Details

This article was originally published as: McKerrow, P, Zhu, S & New, S, Simulating ultrasonic sensing with the lattice gas model, IEEE Transactions on Robotics and Automation, April 2001, 17(2), 202-208. Copyright IEEE 2001.

- [6] M. Erdmann, "Randomization for robot tasks: Using dynamic programming in the space of knowledge states," *Algorithmica*, vol. 10, pp. 248–291, 1993.
- [7] K. Y. Goldberg, "Orienting polygonal parts without sensors," *Algorithmica*, vol. 10, pp. 201–225, 1993.
- [8] L. J. Guibas, R. Motwani, and P. Raghavan, "The robot localization problem," in *Proc. 1st Workshop on Algorithmic Foundations of Robotics*, K. Goldberg, D. Halperin, J.-C. Latombe, and R. Wilson, Eds., Wellesley, MA, 1995, pp. 269–282.
- [9] I. Kamon and E. Rivlin, "Sensory-based motion planning with global proofs," *IEEE Trans. Robot. Automat.*, vol. 13, pp. 814–822, Dec. 1997.
- [10] I. Kamon, E. Rivlin, and E. Rimon, "Range-sensor based navigation in three dimensions," in *Proc. IEEE Int. Conf. Robotics and Automation*, 1999.
- [11] K. N. Kutulakos, C. R. Dyer, and V. J. Lumelsky, "Provable strategies for vision-guided exploration in three dimensions," in *Proc. IEEE Int. Conf. Robotics and Automation*, 1994, pp. 1365–1371.
- [12] J.-C. Latombe, *Robot Motion Planning*. Boston, MA: Kluwer, 1991.
- [13] S. M. LaValle, "A Game-Theoretic Framework for Robot Motion Planning," Ph.D. dissertation, Univ. Illinois, Urbana, 1995.
- [14] S. M. LaValle and J. Hinrichsen, "Visibility-based pursuit-evasion: An extension to curved environments," in *Proc. IEEE Int. Conf. Robotics and Automation*, 1999, pp. 1677–1682.
- [15] S. M. LaValle, D. Lin, L. J. Guibas, J.-C. Latombe, and R. Motwani, "Finding an unpredictable target in a workspace with obstacles," in *Proc. IEEE Int. Conf. Robotics and Automation*, 1997, pp. 737–742.
- [16] S. M. LaValle, B. Simov, and G. Slutzki, "An algorithm for searching a polygonal region with a flashlight," in *Proc. ACM Annu. Symp. Computational Geometry*, 2000.
- [17] J.-H. Lee, S. Y. Shin, and K.-Y. Chwa, "Visibility-based pursuit-evasions in a polygonal room with a door," in *Proc. ACM Annu. Symp. Computational Geometry*, 1999.
- [18] T. Lozano-Pérez, "Spatial planning: A configuration space approach," *IEEE Trans. Comput.*, vol. C-32, no. 2, pp. 108–120, 1983.
- [19] V. Lumelsky and S. Tiwari, "An algorithm for maze searching with azimuth input," in *Proc. IEEE Int. Conf. Robotics and Automation*, 1994, pp. 111–116.
- [20] V. J. Lumelsky and A. A. Stepanov, "Path planning strategies for a point mobile automaton moving amidst unknown obstacles of arbitrary shape," *Algorithmica*, vol. 2, pp. 403–430, 1987.
- [21] M. S. Manasse, L. A. McGeoch, and D. D. Sleator, "Competitive algorithms for on-line problems," in *Proc. ACM 20th Annu. Symp. Theory Comput.*, 1988, pp. 322–333.
- [22] T. D. Parsons, "Pursuit-evasion in a graph," in *Theory and Application of Graphs*, Y. Alavi and D. R. Lick, Eds. Berlin, Germany: Springer-Verlag, 1976, pp. 426–441.
- [23] S. Petitjean, D. Kriegman, and J. Ponce, "Computing exact aspect graphs of curved objects: algebraic surfaces," *Int. J. Comput. Vis.*, vol. 9, pp. 231–255, Dec. 1992.
- [24] M. Pocchiola and G. Vegter, "The visibility complex," *Int. J. Comput. Geom. Applicat.*, vol. 6, no. 3, pp. 279–308, 1996.
- [25] E. Rimon and J. Canny, "Construction of C-space roadmaps using local sensory data—what should the sensors look for?," in *Proc. IEEE Int. Conf. Robotics and Automation*, 1994, pp. 117–124.
- [26] B. Simov, G. Slutzki, and S. M. LaValle, "Pursuit-evasion using beam detection," in *Proc. IEEE Int. Conf. Robotics and Automation*, 2000.
- [27] I. Suzuki and M. Yamashita, "Searching for a mobile intruder in a polygonal region," *SIAM J. Comput.*, vol. 21, no. 5, pp. 863–888, Oct. 1992.
- [28] R. Talluri and J. K. Aggarwal, "Mobile robot self-location using model-image feature correspondence," *IEEE Trans. Robot. Automat.*, vol. 12, pp. 63–77, Feb. 1996.
- [29] M. Yamashita, H. Unemoto, I. Suzuki, and T. Kameda, "Searching for mobile intruders in a polygonal region by a group of mobile searchers," Dept. Elec. Eng. Comput. Sci., Univ. Wisconsin, Milwaukee, TR-96-07-01, 1996.

Simulating Ultrasonic Sensing with the Lattice Gas Model

Phillip John McKerrow, Shao-Min Zhu, and Stephen New

Abstract—People have difficulty understanding ultrasonic sensing because they cannot see sound. The purpose of simulation is to overcome this problem by visualizing the scattering of ultrasonic waves off objects. The lattice gas model calculates wave behavior with finite difference equations to produce data suitable for grayscale visualization. This visualization is useful when designing ultrasonic sensing systems for navigating mobile robots. Situations that result in the sensor failing to detect an object can be studied with the simulator.

Index Terms—Lattice gas model, mobile robot, ultrasonic sensing, wave simulation.

I. INTRODUCTION

Many mobile robots use ultrasonic sensors to detect objects for collision avoidance and navigation. Most of these sensors detect the echo from objects with simple threshold circuits. When the echo amplitude is below the threshold, the object is not detected and the robot may collide with it. The purpose of our research is to solve these problems by understanding the physics of echolocation.

In ultrasonic sensing, high-frequency sound waves are emitted from a transmitter, travel through the air, scatter off objects, and return to a receiver. Signal loss in any of these stages can cause an object to be undetected.

A transducer has a strong main lobe with weaker side lobes. The width of the beam and the strength of the side lobes is one factor in determining which objects produce detectable echoes. Increasing the power of the transducer may result in the detection of an echo from a side lobe. Increasing the beam angle will result in a larger field of insonification and potentially the detection of more objects.

The main cause of signal loss is that the surfaces of the insonified object may reflect most of the energy away from the receiver. An important goal of research into ultrasonic sensing is to determine whether there are situations where no signal is reflected back to the receiver. In these situations, ultrasonic sensing cannot detect the object. A second goal is to develop algorithms to separate low amplitude echoes from noise to produce a useful detection signal.

To achieve these goals, we need to study what happens to the waves when they impact objects. This microscopic view is very difficult to obtain with measurement, because a microphone may interfere with the waves we are trying to measure, particularly when it is close to the reflecting object.

Development of ultrasonic sensing has been slow because people find ultrasonic sensing difficult to understand. As a consequence, simulation plays an important role because it enables us to visualize the sound waves that we cannot see. As we watch waves propagate across a screen and bounce off objects, we begin to grasp the nature of echolocation.

Macroscopic simulations produce animated displays of the wave front. McKerrow and Zhu [13], [14] use an arc model to visualise wave propagation and reflection. Krose and Dondrop [10] and Kimoto

Manuscript received June 14, 2000; revised November 21, 2000. This paper was recommended for publication by Associate Editor J. Leonard and Editor S. Hutchinson upon evaluation of the reviewers' comments.

The authors are with the School of Information Technology and Computer Science, University of Wollongong, NSW 2522 Australia (e-mail: phillip@uow.edu.au).

Publisher Item Identifier S 1042-296X(01)04815-7.

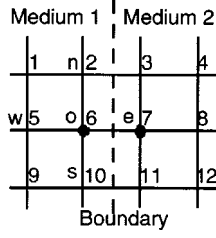


Fig. 1. Grid of cells used in lattice gas model.

and Yuta [7] use ray models to visualise the path of an ultrasonic beam as a mobile robot moves around a simulated environment.

Kuc and Siegel [12] simulated the echoes from specular walls, corners, and edges with impulse models. Vaataja *et al.* [19] use the image source method to compute the propagation paths of ultrasonic beams in three-dimensional environments. In contrast, Teimoorzabeh [17] simulates the echolocation process of bats with biological models of the bat's brain.

Microscopic simulations model the waves and their physical interaction with objects with continuous or discrete mathematics [20], [21], [22]. Continuous models give very accurate results but each wave motion phenomena is modeled separately and the results combined using superposition.

Discrete models achieve more rapid computation, at the expense of accuracy, by modeling the environment as a grid of cells and calculating the wave pressure in each cell using finite difference methods. Also, the computation time is less dependent on the complexity of the environment. However, they are limited to small regions of space because the computation time is proportional to the size of the grid.

Pomeroy *et al.* [16] developed a simulation using the transmission line matrix (TLM) model. TLM is an electrical analogue that captures all wave phenomena. Like TLM, the lattice gas model captures all wave phenomena (propagation, interference, reflection, and diffraction), but it is based on a physical model of wave motion.

The lattice gas model uses a grid to represent points in space. Values of pressure are calculated at every grid cell at each time step of the simulation. The pressure at a lattice point is affected by the recent trends of changing pressure at that point and at neighboring lattice points. The propagation of a wave through the lattice is analogous to Huygen's principle for the construction of wave fronts.

II. LATTICE GAS MODEL

The lattice gas model was developed by Hardy *et al.* [6] to rapidly calculate the Navier–Stokes equation in simulations of fluid flow. Kadanoff and Swift were the first to apply it to modeling wave motion [5]. They used a continuous-time model of particle motion between cells in a grid [3]. Krutar *et al.* [11] extended this work to develop a discrete time model of wave motion by combining groups of particles into differential pressures that propagate through the network.

The environment is modeled as a network of cells (Fig. 1). In this paper, we only consider cells connected in a square grid. A set of equations that represent the state of the environment at each cell is calculated every iteration of the simulation. Possible states include sound source, media [1 . . . n], media boundary, and simulation window edge.

The acoustic wave equation [(1)] relates the wave pressure P with respect to time to the wave pressure with respect to the position of the particles that move to propagate the wave (c is the speed of sound).

$$\frac{\partial^2 P}{\partial t^2} = c^2 \nabla^2 P. \quad (1)$$

The lattice gas model is a finite difference solution [(2)] of the acoustic wave equation, which calculates the pressure at each cell every time step of the simulation [4].

$$dP(x, t + dt/2) = P(x, t + dt) - P(x, t) \quad (2a)$$

$$ddP(x, t) = dP(x, t + dt/2) - dP(x, t - dt/2) \quad (2b)$$

$$ddP(x, t) = \sum_a m_a P(x + dx_a, t) \quad (2c)$$

where $P(x, t)$ is the pressure at time t and location x , and is equivalent to an integer number of particles, dt is the time step, a is a subscript that represents one of the four directions in the grid: north n , south s , east e , west w ; at the cell o (Fig. 1), m_a is a weighted coefficient of the pressure in the direction a , and $m_0 = -c_x^2$, c_x is the speed of sound at cell x , and dP is the pressure difference as a function of time.

The discrete form of the wave equation [(2c)] is derived from the continuous form as follows. First, define

$$m_N = m_S = m_E = m_W = c^2 \quad \text{and} \quad m_0 = -c^2 \quad (3)$$

where c is the speed of sound in the medium.

Next, rewrite the summation in (2c) as

$$\begin{aligned} & m_E P(x + dx_E, t) + m_W P(x + dx_W, t) + 2m_0 P(x + dx_0, t) \\ & + \frac{m_N P(x + dx_N, t) + m_S P(x + dx_S, t) + 2m_0 P(x + dx_0, t)}{d^2 y} \\ & = c^2 \left[\frac{P(x + dx_E, t) + P(x + dx_W, t) - 2P(x + dx_0, t)}{d^2 x} \right. \\ & \left. + \frac{P(x + dx_N, t) + P(x + dx_S, t) - 2P(x + dx_0, t)}{d^2 y} \right]. \quad (4) \end{aligned}$$

With a Taylor series expansion, find the finite difference form of the second-order partial derivative of P with respect to (x, y)

$$\begin{aligned} & \frac{\partial^2 P(x, y, t)}{\partial x^2} + \frac{\partial^2 P(x, y, t)}{\partial y^2} \\ & \cong \frac{P(x + dx, y, t) + P(x - dx, y, t) - 2P(x, y, t)}{d^2 x} \\ & + \frac{P(x, y + dy, t) + P(x, y - dy, t) - 2P(x, y, t)}{d^2 y}. \quad (5) \end{aligned}$$

Therefore, (4) can be rewritten as

$$\begin{aligned} & m_E P(x + dx_E, t) + m_W P(x + dx_W, t) + 2m_0 P(x + dx_0, t) \\ & + \frac{m_N P(x + dx_N, t) + m_S P(x + dx_S, t) + 2m_0 P(x + dx_0, t)}{d^2 y_{(2c)}} \\ & \cong c^2 \left[\frac{P(x + dx_a, t)}{d^2 x} + \frac{P(x + dx_a, t)}{d^2 y} \right] \quad (6) \end{aligned}$$

and the right-hand side of (2c) can be regarded as a discrete form of the wave equation. From (2a), we obtain

$$dP(x, t - dt/2) = P(x, t) - P(x, t - dt). \quad (7)$$

Substitute (2a) and (7) into the right-hand side of (2b) to get

$$\begin{aligned} ddP(x, t) & = P(x, t + dt) - P(x, t) - (P(x, t) - P(x, t - dt)) \\ & = P(x, t + dt) - 2P(x, t) + P(x, t - dt). \quad (8) \end{aligned}$$

Equate (2c) and (8), and rewrite as

$$P(x, t + dt) = 2P(x, t) - P(x, t - dt) + \sum_a m_a P(x + dx_a, t). \quad (9)$$

Replace m_a [(3)] and derive its two-dimensional form

$$\begin{aligned} P_0(t + 1) & = 2P_0(t) - P_0(t - 1) - 4c_{s0}^2 P_0(t) \\ & + c_{sw}^2 P_w(t) + c_{se}^2 P_e(t) + c_{sn}^2 P_n(t) + c_{ss}^2 P_s(t) \quad (10) \end{aligned}$$

where $P_0(t)$ is the wave pressure at location x and time t , c_{s0} is the simulation speed (cells propagated/simulation step) at location x .

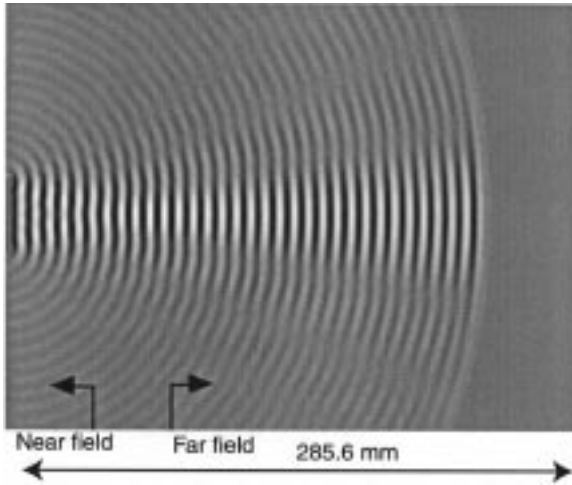


Fig. 2. Visualization of a Polaroid sensor showing main beam and side lobes, calculated on a 840×630 cell grid, with 20 cells/wavelength (6.8 mm). The Polaroid transmitter is the line on the left—104 point source cells.

Equation (10) is a discrete form of the wave equation. It discards higher-order terms in the Talyor series expansion so it does not implement it completely. As a result, some noise has been brought into the results.

III. SIMULATION ALGORITHM

In the algorithm, we combined the three steps [(2a)–(2c)] of Krutar's model into one iterative formula [(10)]. The simulation uses a two-dimensional cross grid topology. The maximum simulation speed is 0.707 cells/time step [11], which represents isotropic sound propagation at the slowest data flow speed limit along the diagonals of the grid cells. The maximum speed of sound in any medium in the simulation is equivalent to this rate.

Initially, the pressure in every cell is set to zero. The user specifies the frequency (f), the spatial resolution (model scale) and the medium used in the simulation. From this, the simulator calculates the simulation rate, based on the maximum speed of sound (c_{\max}) in any part of the medium.

$$\text{simulate rate } R = \frac{c_{\max} * S}{0.707} \text{ steps/second} \quad (11)$$

$$\text{model scale } S = \frac{m * f}{c_{\max}} \text{ cells/meter} \quad (12)$$

where m is the number of cells/wavelength.

The image in Fig. 2 uses an 840×630 grid and 20 cells/wavelength. At 50 kHz, the physical wavelength is 6.8 mm and the width of the image is a distance of 286.5 mm.

IV. SIMULATING A TRANSMITTER

Ultrasonic transducers emit a spherical wave front but, the transducer focuses the energy into a beam with side lobes (Fig. 2). The beam angle (directivity function) is a function of the physical dimensions of the transducer [8]. When emitting at 50 kHz, the beam angle of the Polaroid transducer is 15° from the axis to the minimum between the main beam and the first side lobe [1]. Also, the shape of the wave front is flat in the near field and becomes spherical in the far field.

A transducer is modeled as a line of vibrating cells with length equal to the diameter of the transducer. The lobe pattern in the far field is clearly seen in the visualization in Fig. 2, where each source cell has the same pressure amplitude. By weighting the pressure in the end cells, the simulated lobe pattern can be adjusted to approximate the measured lobe patterns. The aim of weighting is to move the minima to the correct angles and to adjust the amplitudes of the side lobes to the correct

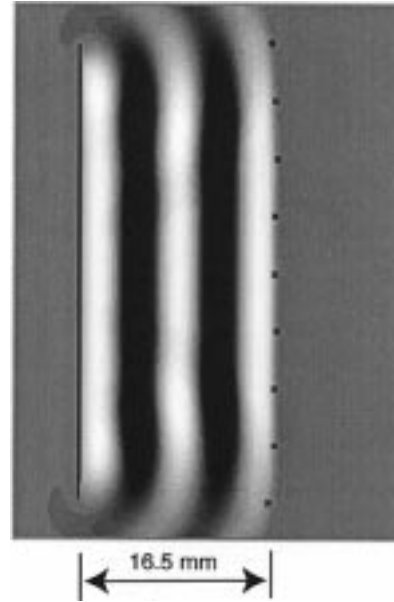


Fig. 3. Wave front of main lobe in the near field of Polaroid sensor. Crosses indicate the measured position of the wave front 16.5 mm from transducer. Source cells at both ends of the transducer have been delayed by up to 18° .

values. To achieve a close match to the measured response, it may be necessary to change the diameter of the transducer in the simulation, as the diameter of the vibrating portion of the transducer may be different to the physical diameter.

The second parameter to be considered when simulating a transducer is the shape of the wave front. We found that, in the near field, the sides of the main lobe were further from the transducer in the simulation than in our measurements (Fig. 3). This difference in wave shape can be corrected in the simulation by giving the source cells at the sides of the transducer a phase lag. Physically, this is equivalent to the elemental vibrating cells at the periphery of the transducer having a higher capacitance than those in the middle.

V. IMPEDANCE CHANGES AT BOUNDARIES

The lattice gas model simulates wave propagation, interference, reflection, refraction, and diffraction. Refraction is of little interest because the high impedance difference between air and solid objects results in most of the energy being reflected. The wave equation models propagation and interference. Diffraction is the gradual spreading out of sound waves. It is simulated by the fact that each cell is a weighted sum of its neighbors.

Reflection occurs when the impedance of the medium changes at a boundary. At such a boundary, the speed of sound and the acoustic impedance change. Equation (10) only models the change of speed. To model the change of impedance, the boundary cell calculations must include values for the reflection and transmission coefficients.

The amount of energy reflected at a boundary, and hence the amount transmitted through the boundary, is a function of the relative impedances of the two media and the incident angle. The pressure reflection coefficient R_{12} for waves travelling from medium 1 to medium 2 is [2]

$$R_{12} = \frac{Z_2 - Z_1}{Z_2 + Z_1} \quad (14)$$

where Z_1 is the impedance in the medium 1.

For example, the reflection coefficient R_{12} for the air to pine interface is 0.9995. The pressure transmission coefficient for waves travelling from medium 1 to medium 2 is

$$T_{12} = \frac{2Z_2}{Z_2 + Z_1} = 1 + R_{12} \quad (15)$$

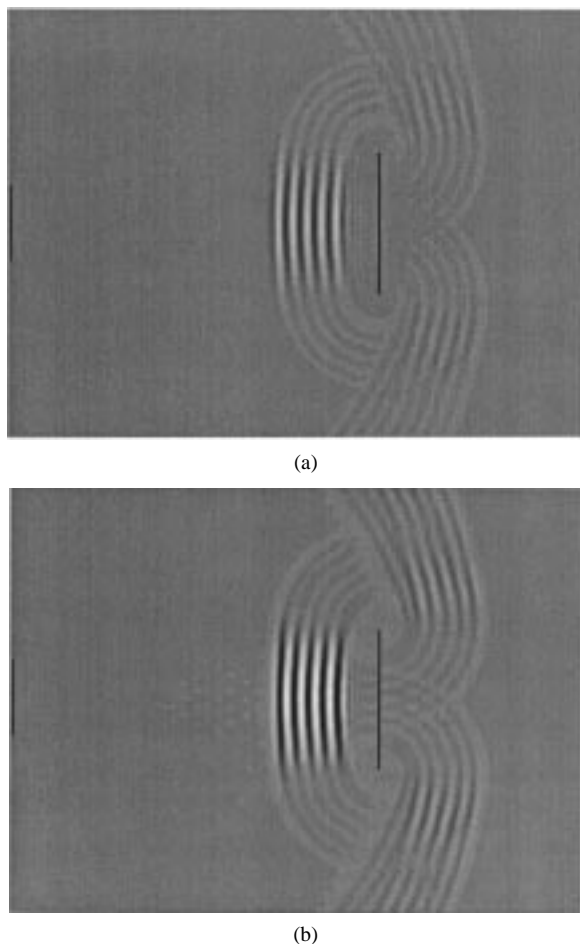


Fig. 4. Reflection, transmission and diffraction of waves at a specular surface. (a) Surface modeled by setting the speed of sound in the object to zero. (b) Surface modeled by setting $R_{12} = 1$ and $T_{21} = 0$ in (18).

The effects due to impedance changes at boundaries are modeled by including these coefficients in the equations for the boundary cells. A smooth boundary is modeled with a straight line between cells as shown in Fig. 1. Such a boundary should cause specular reflection. Consider cell 6 in Medium 1 next to the boundary. Applying the Lattice Gas model [(10)] to this cell gives a pressure of:

$$P_6(t+1) = 2P_6(t) - P_6(t-1) - 4c_6^2 P_6(t) + c_2^2 P_2(t) + c_5^2 P_5(t) + c_{10}^2 P_{10}(t) + c_7^2 P_7(t). \quad (16)$$

The last term in (16), $c_7^2 P_7(t)$, is the component from the boundary. One way of modeling a specular reflector is to set the speed of sound in the surface [c_7 in (16)] to zero [Fig. 4(a)], which causes all the energy that impinges on the boundary to be absorbed. However, this does not take into account the impedance of the two media. The component from the boundary is composed of two parts: one transmitted from cell 7, and the other reflected from cell 6 itself. This term is replaced by

$$c_6^2 R_{12} P_6(t) + c_7^2 T_{21} P_7(t). \quad (17)$$

Substitute (17) into (16) to obtain the lattice gas model equation for cell 6

$$P_6(t+1) = 2P_6(t) - P_6(t-1) - 4c_6^2 P_6(t) + c_2^2 P_2(t) + c_5^2 P_5(t) + c_{10}^2 P_{10}(t) + c_6^2 R_{12} P_6(t) + c_7^2 T_{21} P_7(t) \quad (18)$$

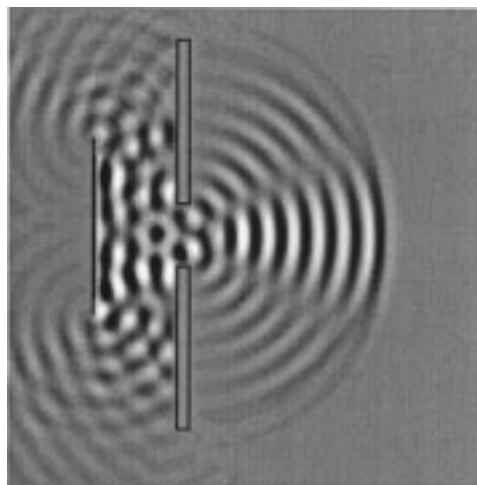


Fig. 5. Diffraction, reflection, and interference that occur when waves pass through a small gap.

Similarly, the equation for the pressure at cell 7 is

$$P_7(t+1) = 2P_7(t) - P_7(t-1) - 4c_7^2 P_7(t) + c_3^2 P_3(t) + c_8^2 P_8(t) + c_{11}^2 P_{11}(t) + c_7^2 R_{21} P_7(t) + c_6^2 T_{12} P_6(t). \quad (19)$$

A physically correct method for modeling a specular surface that reflects all the energy is to set the reflection coefficient to 1 and the transmission coefficient to 0 in (18). As shown in Fig. 4(b), the visualization appears the same as in Fig. 4(a), except that the phase of the reflected waves has not been reversed. Also, the pressure amplitudes are different, because (18) contains a term for the energy reflected from the boundary, which reduces the c_6 coefficient from 4 to 3.

When the impedance decreases at the boundary, phase reversal occurs [(14)] and the reflection coefficient is negative, for example, at a water to air interface. In contrast, when the impedance increases at the boundary, the phase of the reflected wave is unchanged and the reflection coefficient is positive, for example, an air to object interface.

One advantage of the physically correct model [(18)] is that it can be used within a medium by setting the transmission coefficient to 1 and the reflection coefficient to zero. As a result, (18) reduces to (10). Thus, we have a general equation for cells within media and on media boundaries.

When the complete lattice gas model [(18)] is used, all wave phenomena can be simulated and visualized. Fig. 5 shows wave propagation, reflection, interference, and diffraction for waves passing through a narrow opening.

VI. MODEL VALIDATION

The usefulness of a simulation is determined by the approximations used in its calculations, how well the model fits the physics, and the clarity with which the visualization conveys the parameters of interest. Errors in any of these three areas can reduce the quality of the simulation.

The lattice gas model is a finite difference approximation of the wave equation. Cole [4] analyzed the errors introduced into the wave equation by finite difference approximations. Solution errors can be reduced by using finer spaced time sampling of the wave field at the cost of increased computation, or with more complex equations.

We presented some measurements (Fig. 3) to show how the simulation can be adjusted to accurately model the shape of the wave front generated by a transducer. Other transducer parameters, including lobe

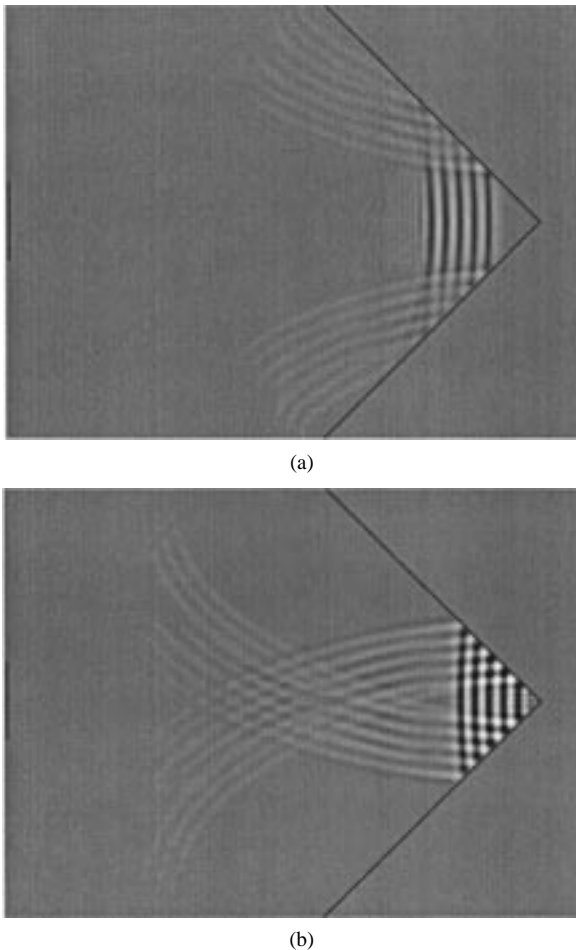


Fig. 6. Waves reflecting from a concave corner at (a) the 1030th simulation step and (b) the 1300th step.

pattern [1], angular frequency response, and transmitted wave shape [18] were also measured with a microphone.

We have made measurements of the reflections from objects [18] at points in the sound field. However, measuring images of sound fields with a microphone for comparison to those generated by the simulation is impossible. First, the simulations produce data for every cell in an 840×630 grid. To obtain a similar image by measurement requires placing a microphone in 529 200 positions. The second problem is more significant: placing the microphone in many of the desirable measurement positions results in the transmitted beam reflecting off it, which changes the sound field, and invalidates the measurement, particularly near boundaries.

We validated the visualization by visually comparing it to images of water waves in ripple tanks and real environments, and to images of light and water waves in physics books. We have enjoyed many hours watching waves on beaches and in harbors. Using this visual analog to verify the visualization is validated by the photographs of sound waves produced by Winston Kock [9]. He attached a light to a scanning microphone and modulated its brilliance proportional to the measured sound field. He recorded the intensity of the light with a time-lapse camera as the microphone was scanned in a vertical plane.

VII. APPLICATION TO ROBOTICS

In robotics, we wish to visualize reflections off common geometric features when insonified by an ultrasonic transmitter. In Figs. 2 and 3, the output of a Polaroid sensor is visualised, showing the beam both

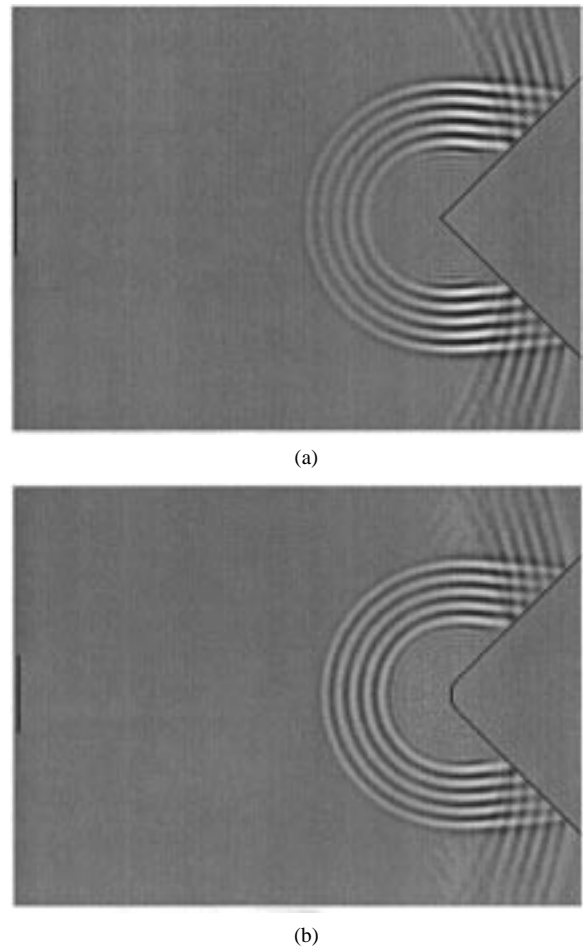


Fig. 7. Reflection of beam from convex edge: (a) sharp edge and (b) rounded edge.

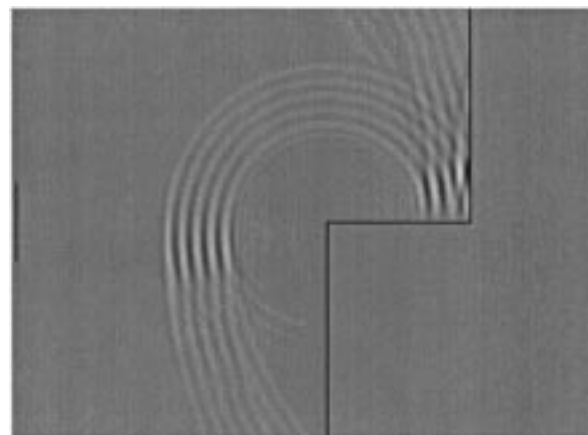


Fig. 8. Reflection of beam from a stepped surface.

in the near and far fields. In the far field, the beam spreads to give a conical field of audition.

Figs. 6–10 show visualizations of typical sensing situations that occur in mobile robotics. Ultrasonic pulses 5 cycles long are transmitted by a transducer situated at the left of the image.

Mobile robot's that map environments with ultrasonic sensors have to deal with the problem that the echo from a corner has similar characteristics to an echo from a wall at the same range. Fig. 6 shows two images from a time sequence of images for reflection from a convex corner.

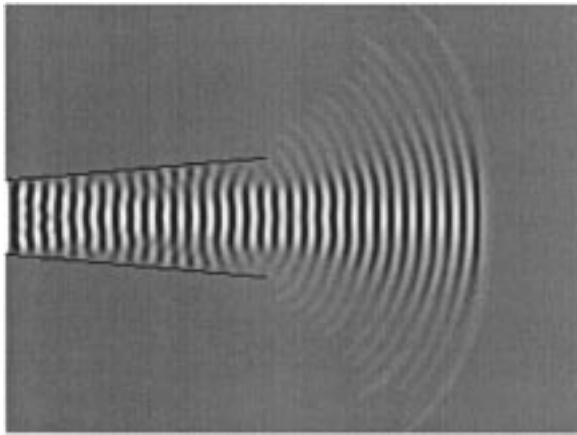


Fig. 9. Beam pattern from a transmitter with a 5° cone shaped horn 125 mm in length.

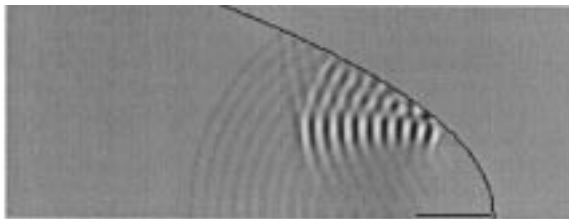


Fig. 10. Reflection of ten cycles off a parabolic reflector with the transmitter at the focal point.

Mobile robot's that detect objects with ultrasonic sensors for collision avoidance have to deal with the problem that the echo from a sharp edge is very small, and most of the energy is reflected away from the sensor. Fig. 7 shows reflection from convex edges with different curvature. Significantly more energy is reflected from the curved edge. In indoor environments, the edges of most objects have enough curvature to produce a significant reflection.

Mobile robot's that follow walls with ultrasonic sensors have to detect steps in a wall, such as a recess for a door. Fig. 8 shows the reflection from a stepped surface. Sufficient energy is reflected from both surfaces for a sensor that detects multiple echoes to find the step.

It is common practice in robotics to use horns and reflectors to produce narrower beams. Fig. 9 shows the effect of a 5° cone 125 mm long on the output of the transducer. In comparison to the sensor without a cone (Fig. 2), the one with the cone produces a much narrower beam.

The ears of some bats focus the energy with a 20-dB gain. A parabola can be used to achieve similar focussing. When the output of transducer is reflected from a parabolic mirror, some defocusing occurs because most of the transducer is not at the focal point of the parabola due to the width of the transducer. By the principle of reciprocity, a similar effect occurs on reception.

Figs. 6–10 were produced with the lattice gas model with 20 cells/wavelength. Surfaces were simulated by setting the speed of sound in the obstacle to zero, which results in phase reversal of the reflected waves. Every third cell is used in the rendering in order to reduce the size of the image.

VIII. CONCLUSION

The lattice gas model can be used for research into ultrasonic sensing for mobile robot applications. It provides a method for simulating the propagation of ultrasonic waves in air that

- 1) enables the visualization of wave phenomena of interest,

- 2) uses a finite difference method to calculate a continuous time physical model,
- 3) models the impedance changes at boundaries,
- 4) produces data suitable for grayscale visualization, and
- 5) has a computation time that is independent of the complexity of the environment being modeled.

The lattice gas model has the limitation that it does not model environment conditions. It assumes that the pressure in all media in the simulation is initialized to zero. Also, it does not model attenuation due to absorption in the medium. It may be possible to model attenuation when calculating the pressure in a cell by weighting the contributions of the four connected cells [(10)] to simulate the exponential decay caused by the medium. For the simulations presented in this paper, the attenuation is negligible.

The model is easy to understand and relatively simple to code. However, time and memory usage increases rapidly with the number of cells per wavelength and the size of the grid. The lattice gas model is inherently parallel and considerable speed up can be achieved on a parallel computer [15]. Animation can be achieved by recording a sequence of images and playing them back at the desired rate.

Simulation of situations that occur in mobile robot applications is a useful tool for understanding ultrasonic sensing. The microscopic view of wave motion that the lattice gas model provides enables a researcher to study the effect of different geometric primitives on the echo. The understanding gained can be used to plan experiments to validate the simulation results and to design sensing systems to detect specific objects. The researcher can simulate different sensor configurations and investigate suitable data analysis algorithms. Using the knowledge gained through simulation, he can design new sensing strategies.

ACKNOWLEDGMENT

The authors would like to thank Apple Computer Australia for providing two Macintosh computers for this research through their Apple University Development Fund.

REFERENCES

- [1] C. Biber, S. Ellen, E. Shenk, and J. Stempeck, "The polaroid ultrasonic ranging system," in *Proc. 67th Convention Audio Eng. Soc.*, 1980.
- [2] W. S. Burdic, *Underwater Acoustic System Analysis*. Englewood Cliffs, NJ: Prentice-Hall, 1984.
- [3] H. Chen, S. Chen, G. Doolen, and Y. C. Lee, "Simple lattice gas models for waves," *Complex Syst.*, vol. 2, pp. 259–267, 1998.
- [4] J. B. Cole, "A nearly exact second order finite difference wave propagation algorithm on a coarse grid," *Comput. Physics*, vol. 8, no. 6, pp. 730–734, 1994.
- [5] U. Frisch, D. d'Humieres, B. Hasslacher, P. Lallemand, Y. Pomeau, and J. Rivet, "Lattice gas hydrodynamics in two and three dimensions," *Complex Syst.*, vol. 1, pp. 649–707, 1987.
- [6] J. Hardy, O. de Pazzis, and Y. Pomeau, "Molecular dynamics of a classical lattice gas: Transport properties and time correlation functions," *Phys. Rev. A*, vol. 13, no. 5, pp. 1949–1961, 1976.
- [7] K. Kimoto and S. Yuta, "A simulation for programming the behavior of an autonomous sensor-based mobile robot," in *Proc. IROS*, Raleigh, NC, 1992, pp. 1431–1438.
- [8] L. E. Kinsler, A. R. Frey, A. B. Coppens, and J. V. Sanders, *Fundamentals of Acoustics*, 3rd ed. New York: Wiley, 1982.
- [9] W. E. Kock, *Seeing Sound*. New York: Wiley, 1971.
- [10] B. J. A. Krose and E. Dondorp, "A sensor simulation system for mobile robots," in *Proc. IAS-2*, Dec. 1989, pp. 641–649.
- [11] R. A. Krutar, S. K. Numrich, R. K. Squier, J. Pearson, and G. Doolen, "Computation of acoustic field behavior using a lattice model," *Oceans*, pp. 446–452, 1991.
- [12] R. Kuc and M. W. Siegel, "Physically based simulation for acoustic sensor robot navigation," *IEEE Trans. Pattern Anal. Machine Intell.*, vol. PAMI-9, no. 6, pp. 766–778, 1987.
- [13] P. J. McKerrow, "Simulation of sonar echolocation," in *Proc. 1st Workshop on Domestic Robotics*, Sept. 1989, pp. 127–136.

- [14] P. J. McKerrow and S. Zhu, "Modeling multiple reflection paths in ultrasonic sensing," in *Proc. IROS'96*, Osaka, Japan, Nov. 1996, pp. 284–291.
- [15] S. K. Numrich, K. Krutar, and R. Squier, "Computation of acoustic fields on a massively parallel processor using lattice gas methods," in *Proc. 3rd IMACS Symp.*, 1991.
- [16] S. C. Pomeroy, H. R. Williams, and P. Blanchfield, "Evaluation of ultrasonic inspection and imaging systems for robotics using TLM modeling," *Robotics*, vol. 9, pp. 283–290, 1991.
- [17] K. Teimoorzabeh, "Seeing in the dark with artificial bats," in *Proc. 3rd Eur. Conf. Artificial Life*, 1995.
- [18] J. Tsakiris and P. J. McKerrow, "An analysis of freedman's "image pulse" model in air," *J. Acoust. Soc. Amer.*, vol. 108, no. 4, pp. 1602–1613, Oct. 2000.
- [19] H. Vaataja, H. Hakala, P. Mattila, and R. Suoranta, "3-D simulation of ultrasonic sensor system in mobile robots," in *Proc Ultrasonics Symp.*, 1992, pp. 333–336.
- [20] S. Zhu and P. J. McKerrow, "Simulation of a ripple tank," *Acoust. Australia*, vol. 23, no. 2, pp. 57–63, 1995.
- [21] —, "Visualization of ultrasonic sensing," in *Proc. 1995 Nat'l. Conf. Australian Robot Association*, 1995, pp. 196–205.
- [22] —, "Visualising the reflection of a curved wavefront off a curved surface," *IEEE Computat. Sci. Eng.*, vol. 5, no. 4, pp. 30–39, Oct.–Dec. 1998.

Nonlinear Controllability and Stability Analysis of Adaptive Image-Based Systems

Fabio Coticelli and Benedetto Allotta

Abstract—In this paper, a novel adaptive visual feedback scheme is presented to solve the problem of controlling the relative pose between a robot camera and a rigid object of interest. By exploiting nonlinear controllability properties, uniform asymptotic stability in the large of the image reference set-point is proved using Lyapunov's direct method. Moreover, uniform boundedness of the whole state vector is ensured by using an adaptive nonlinear control scheme, in case of unknown object depth. Experimental results with a six-degree-of-freedom robot manipulator endowed with a camera on its wrist validate the framework.

Index Terms—Controllability, experimental results, nonlinear depth adaptation, nonlinear visual model, stability analysis.

I. INTRODUCTION

In this paper, the problem of camera-object relative positioning is addressed by nonlinear controllability analysis and adaptive image-based visual servoing.

The advantages of the proposed framework can be summarized as follows.

- The state space representation is fully defined in the image space in terms of two-dimensional (2-D) points, system dynamics is derived using full perspective projection, hence drawbacks (e.g., lack of global properties, ambiguities, image singularities) of linearized camera models are avoided.

Manuscript received June 23, 2000. This paper was recommended for publication by Associate Editor S. Hutchinson and Editor A. De Luca upon evaluation of the reviewers' comments. This paper was presented at the IEEE/ASME International Conference on Advanced Intelligent Mechatronics, Atlanta, GA, September 1999.

The authors are with the Scuola Superiore Sant'Anna, Pisa I-56127, Italy (e-mail: coticelli@sssup.it; ben@sssup.it).

Publisher Item Identifier S 1042-296X(01)04814-5.

- The visual model is characterized by a redundant number n of image points (i.e., the case $n > 3$ is considered), which permits to achieve robust visual tracking, to eliminate bad features (e.g., points which are moving along its projection ray) and to guarantee full-rank of the interaction matrix.
- Stability in the large of camera-object visual interaction model is formally proven as consequence of nonlinear controllability results and Lyapunov's direct method.
- Adaptive depth estimation from 2-D image information is based on stable Lyapunov-based design, ultimate boundedness of the whole state vector is guaranteed, and camera calibration procedure is not required.

Experimental results, obtained with a robotic system consisting in a PUMA 560 endowed with a camera on its wrist (eye-in-hand configuration), show that the proposed approach is feasible in visual servoing applications (e.g., visually guided manipulation, assembly tasks, docking operation), also in case of large change of orientation and translation of the robot camera.

The paper is organized as follows. In Section I-A, works close to our approach are briefly summarized, and differences are highlighted. In Section II, the visual model is introduced, controllability analysis, and consequent results are presented. In Section III, the adaptive nonlinear control system is designed and stability analysis is carried out. Section IV reports real robotic experiments. Finally, in Section V the major contribution of the paper is summarized.

Notations: $\mathcal{A} \setminus \mathcal{B}$ denotes subtraction between sets \mathcal{A} and \mathcal{B} , $\mathcal{B}(\mathbf{x}, r) = \{\mathbf{x} \in \mathbb{R}^n : \|\mathbf{x}\| \leq r\}$, $r > 0$, is a closed ball in \mathbb{R}^n , $I_n \in \mathbb{R}^{n \times n}$ denotes the identity matrix, $0_{n \times m} \in \mathbb{R}^{n \times m}$ is a matrix of zeros, $\text{diag}(x_i) \in \mathbb{R}^{n \times n}$ is the diagonal matrix with the elements of $\mathbf{x} = [x_1 \dots x_n]^T \in \mathbb{R}^n$, $\text{so}(3)$ denotes the vector space of the skew-symmetric matrices of order 3, an element of $\text{so}(3)$ is indicated with \mathbf{x}^\wedge , where $\mathbf{x} \in \mathbb{R}^3$. $\text{SE}(3) = \mathbb{R}^3 \times \text{SO}(3)$ denotes the special Euclidean group, where $\text{SO}(3)$ denotes the special orthogonal group. Given a vector space V on the field \mathbb{R} , $\forall \mathbf{v}, \mathbf{w} \in V$, $\langle \mathbf{v}, \mathbf{w} \rangle$ denotes their Euclidean scalar product and $\|\cdot\|$ is the usual Euclidean norm. \oplus denotes the direct sum of vector spaces.

A. Related Work

In the last few years, several control schemes have been proposed to solve the problem of robot positioning and tracking, with respect to salient features in the environment, using visual information in the control loop. Here, the works close to our approach are briefly summarized, differences and drawbacks are highlighted. In [1], a general image-based methodology is proposed in which the interaction matrices of several primitives (points, lines, planes, circles, spheres) are derived. The proposed control scheme is a particular case of the more general framework presented in [2]. Three dimensional (3-D) parameters are usually unknown, the authors propose to fix these quantities to constant values, i.e., a value corresponding to the desired pose or to a generic estimate. Hence, asymptotic stability is ensured only in a local neighborhood of the desired configuration. Global stability issues are not investigated and depth parameters adaptation is not considered. A series of works, done by the research group of Carnegie Mellon, consider the same problem investigated in our framework. In [3], the problem of real-time visual tracking is solved using an eye-in-hand robot configuration. It turns out that simple PI controllers can be applied in case of accurate visual tracking, in the pole assignment scheme the selection of closed-loop poles should be done carefully due to possible instabilities, LQG can be used to take into account inaccurate measurements, but at the cost of noticeable increase of system complexity. In [4] and [5], the same problem of [3] is considered, but in